Aeroacoustic performance of a seal vibrissa shaped cylinder ⊘

Tom A. Smith ⓘ ; Guanjiang Chen; Bin Zang ⓘ

Check for updates

CrossMark

View Online   Export Citation

Related Content

Three-dimensional spectral proper orthogonal decomposition analyses of the turbulent flow around a seal-vibrissa-shaped cylinder

Physics of Fluids (February 2021)

Effect of the orientation of the harbor seal vibrissa based biomimetic cylinder on hydrodynamic forces and vortex induced frequency

AIP Advances (October 2017)

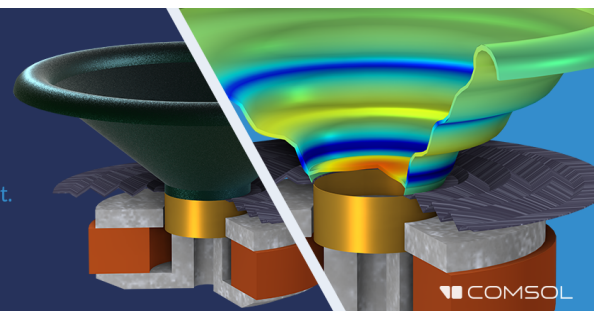The frequency response of rat vibrissae to sound

J. Acoust. Soc. Am. (May 2008)

JASA

ARTICLE

Aeroacoustic performance of a seal vibrissa shaped cylinder

Tom A. Smith,[1,a] Guanjiang Chen,[2] and Bin Zang[2]

[1]*Department of Mechanical Engineering, University College London, Gower Street, London, WC1E 6BT, United Kingdom*

[2]*Faculty of Engineering, University of Bristol, Bristol, BS8 1TR, United Kingdom*

ABSTRACT:

Bio-inspired geometries have many applications in engineering, including in the field of noise control. In this work, the aeroacoustic performance of a seal vibrissa shaped cylinder (SVSC) is investigated and compared to that of a circular cylinder at Re $= 37\,000$. Experiments conducted in an anechoic wind tunnel are compared to results from a hybrid aeroacoustic simulation with excellent agreement observed between the two. The overall sound pressure level is found to be 24.3 dB lower for the SVSC, and no prominent narrowband component is observed in the acoustic spectrum. Analysis of the flow field and surface pressure fluctuations reveals that this is because the usual large-scale alternating vortex shedding realized for bluff body flows is absent for the SVSC. Instead, smaller uncorrelated vortices are shed from the upper and lower sides of the geometry, which, when combined with a lower spanwise correlation, results in a much lower acoustic intensity spread over a broader frequency range.
© 2023 Acoustical Society of America. https://doi.org/10.1121/10.0020912

I. INTRODUCTION

Bluff body flows are responsible for significant noise levels across a range of applications, for example, in aircraft landing gear and train pantographs. Most commonly associated with tonal or narrowband noise from coherent vortex shedding, bluff bodies can also be responsible for significant levels of interaction noise (Jacob *et al.*, 2005). In such cases, the bluff body acts an acoustic source and creates fluctuations in the flow which impinge on other geometries, generating additional noise. Due to the large amplitude noise that can be generated and the ubiquity of bluff bodies in engineering applications, there is a need to develop geometries that produce less flow-induced noise.

Biologically inspired geometries have much potential in the field of noise control with many animals having developed unique adaptations that enable them to hunt almost silently or avoid predators. Such geometries have been extensively explored for lifting surface noise control, often focusing on serrated or porous edges and wavy surface geometries. Much inspiration has been taken from owl feathers, the unique structure of which enables them to fly almost silently (Graham, 1934; Wagner *et al.*, 2017). This has inspired numerous modifications to airfoil geometries, including porous surfaces and serrated edges (Clark *et al.*, 2016; Wang *et al.*, 2021). Several studies (Agrawal and Sharma, 2016; Chen *et al.*, 2018) have found that wavy or serrated leading edges can reduce interaction noise by reducing the scattering efficiency of the leading edge. At moderate Reynolds numbers, wavy geometries combined with serrated edges have also been shown to reduce trailing edge noise (Wang *et al.*, 2017) by reducing the spanwise correlation of the Tollmien-Schlichting instability waves in the boundary layer. Smith and Klettner (2022) showed that a wavy surface could eliminate tonal instability noise by superimposing two regular waves to create a more irregular surface. Use of a double-wavy geometry was also found to lead to better reductions in leading edge noise (Chaitanya *et al.*, 2018). However, far less research has been conducted into how bio-inspired geometries might be used to control bluff body noise.

In the context of bluff body noise control, one geometry of particular interest is the vibrissae of the harbour seal (*Phoca vitulina*). Seals use their vibrissae for identifying objects, either by touch or sensing disturbances in the water, which enables them to locate prey. The harbour seal vibrissae have a unique wavy geometry that is not found in similar species, and Hanke *et al.* (2010) showed that the principal purpose of this unique geometry is to reduce the vortex-induced vibrations that would otherwise impair the seal's ability to detect prey. Several subsequent works have used experimental and computational techniques to investigate the flow around the vibrissa, generally at low subcritical Reynolds numbers, revealing much about the flow field that results from this unique structure. The wake flow fields of seal vibrissa shaped cylinders (SVSCs) were investigated by Wang *et al.* (2017) and Wang and Liu, (2016), and it was presented that the recirculation region behind a vibrissa shaped cylinder is significantly more stable than for a circular cylinder (CC), suppressing the periodic vortex shedding behaviour. A more recent study (Chu *et al.*, 2021) used spectral proper orthogonal decomposition on the flow field around a vibrissa at Re $= 2 \times 10^4$ and identified a number of key features that reduce the fluctuating lift force, which is

a)Email: tom.smith.17@ucl.ac.uk

responsible for vortex-induced vibrations. The results also showed that the wake behind the vibrissa is more stable than that for a CC, leading to a longer vortex formation length and weaker vortex shedding. Furthermore, out-of-phase vortex shedding along the span led to a significant reduction in the lift fluctuations.

The coherent vortex shedding that gives rise to vortex-induced vibrations is the same phenomenon responsible for the production of aeolian tones from cylindrical geometries and other bluff bodies. This tonal noise is caused by the alternating vortex shedding into the wake of the body and is particularly prominent in the subcritical regime. This type of noise has been extensively studied over centuries, and detailed descriptions of the mechanics, acoustic intensities, and relationships between the local flow and far-field noise can be found in many works, for example, Fujita (2010), Inoue and Hatakeyama (2002), Rayleigh (1896), and Revell *et al.* (1978). There are numerous applications, particularly within the transport and energy sectors, where reducing this type of noise is beneficial. One recent study (Chen *et al.*, 2022b) has shown that the SVSC can be effective at suppressing aeolian tones, indicating that it can be an effective passive modification for reducing bluff body noise. Previous works have confirmed that vibrissa shaped cylinders have smaller lift fluctuations than circular and constant cross-section elliptical cylinders (ECs; Jie and Liu, 2017; Yoon *et al.*, 2020). Given the close relationship between lift fluctuations and tonal noise production for cylindrical bodies (Gerrard, 1955; Phillips, 1956), these studies imply that a vibrissa cylinder should produce less noise, but the underlying mechanics and relationship between the flow field and far-field noise have not, yet, been explored in detail.

In this work, computational and experimental methods are used to determine the far-field noise resulting from the flow over a SVSC and compare it to that of a CC. The flow velocity is $U_\infty = 25$ ms^{-1}, which corresponds to a Reynolds number of $Re = 3.7 \times 10^4$ based on the CC diameter. Wind tunnel experiments are conducted to obtain velocity measurements in the near-field and the acoustic pressure in the far-field. These data are used to validate numerical simulations which are conducted using a hybrid aeroacoustic method. Here, incompressible large eddy simulations are used to resolve the turbulent flow field around the geometries and compute the acoustic source terms. These source terms are then mapped onto a larger domain where the acoustic perturbation equations are solved numerically to obtain the acoustic pressure in the far field. The aim of this study is to assess the level of noise suppression by the SVSC compared to that for the circular one and, through detailed flow field analyses from the simulations, show how the noise reduction relates to the dynamics of the fluid flow around the cylinder.

II. METHODS

A. Cylinder geometry

Two geometries are considered in this study: a CC and a SVSC. The cylinder has a diameter of $D = 0.022$ m. The
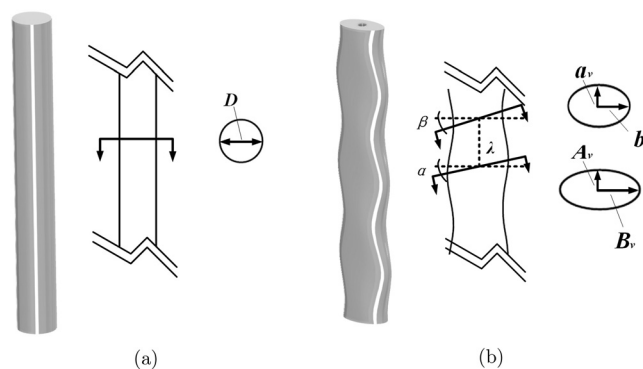

FIG. 1. Geometry of the CC (a) and SVSC (b). The upper ellipse in (b) denotes a saddle plane and the lower ellipse denotes a nodal plane.

experimental span is $L_e = 20D$ and simulation span is $L_s = 10D$. The reduced span used for the simulation is performed for computational expedience, but it still ensures that the span is significantly greater than the spanwise correlation length, as will be shown in Sec. III. The unique geometry of the SVSC can be described in terms of two planes, depicted in Fig. 1, and referred to as nodal and saddle planes. The parameters for this geometry are given in Table I and are chosen such that the total volume of the SVSC is similar to that of the CC. The parameters are the same as those used in existing studies of the fluid dynamics and acoustics of vibrissa shaped cylinders, for example, Chu *et al.* (2021) and Yoon *et al.* (2020), and based on the idealised geometry developed by Hanke *et al.* (2010).

B. Experimental methods

The far-field acoustic measurements were performed at the aeroacoustic wind tunnel facility at University of Bristol. The facility is a closed-loop open-jet wind tunnel and anechoic down to 160 Hz. The open-jet nozzle has an exit dimension of 0.5 m in width and 0.775 m in height. Two side plates were secured to the sides of the nozzle exit and the cylinder was mounted at the vertical centre of the nozzle, 0.6 m away from the exit plane. The far-field acoustics were captured by an overhead microphone array, 1.75 m from the centre of the cylinder and the data were sampled simultaneously at sampling rate of 2^{15} Hz using NI-DAQ system (National Instruments, Austin, TX). More details of the wind tunnel noise and flow characteristics can be found in (Mayer *et al.*, 2019).

To quantify the flow field, the same cylinder was then mounted with side plates in a low turbulence wind tunnel, where the velocity fields in the cylinder wake were captured by a two-dimensional, two-component time-resolved particle-image velocimetry (PIV) system. The wind tunnel has a test section similar to that of the aeroacoustic facility and, hence,

TABLE I. Geometric parameters for the SVSC.

λ (mm)	a_v (mm)	b_v (mm)	A_v (mm)	B_v (mm)	α (°)	β (°)
27.5	8.6	14.3	7.3	17.8	15.3	17.6

produces a comparable blockage ratio of approximately 2.8% with the circular baseline cylinder. The PIV images were captured by a Photron FASTCAM Mini WX-100 double-frame camera (Tokyo) with a resolution of 2048×2048 pixel^2 and sampling frequency of 840 Hz. The images were then subjected to multi-pass cross correlation and a global vector validation scheme to yield the final velocity fields of $132\,\mathrm{mm} \times 106\,\mathrm{mm}$ with a spatial resolution of 0.88 mm. Further information on the experimental measurements can be found in Chen *et al*. (2022a) and Liu *et al*. (2022). The two test facilities are displayed in Fig. 2.

C. Numerical methods

The computational modelling is performed by way of a hybrid aeroacoustic approach, where the incompressible fluid fields are obtained using a large eddy simulation. The resolved flow field is then used to compute acoustic source terms, which are interpolated onto a larger, partially overlapping acoustic domain. The acoustic perturbation equations are then solved on this domain to obtain the three-dimensional acoustic pressure field.

The fluid is modelled as viscous, incompressible, and Newtonian. Wall-resolved large eddy simulations are used, and the governing equations for the spatially filtered pressure and velocity fields are given in Eqs. (1) and (2):

$$\frac{\partial \overline{U_i}}{\partial x_i} = 0, \tag{1}$$

$$\frac{\partial \bar{U}_j}{\partial t} + U_j \frac{\partial \bar{U}_i}{\partial x_i} = -\frac{1}{\rho}\frac{\partial \bar{p}}{\partial x_j} + \nu \frac{\partial^2 \bar{U}_j}{\partial x_i \partial x_i} - \frac{\partial \tau_{ij}}{\partial x_i}, \tag{2}$$

where the sub-filter scale stresses, τ_{ij}, are given by

$$\tau_{ij} = \overline{U_i U_j} - \bar{U}_i \bar{U}_j. \tag{3}$$

Equations (1)–(3) are closed using the one-equation dynamic k sub-filter scale model (Kim and Menon, 1995), which has been observed in previous studies of foil and bluff bodies (Smith and Ventikos, 2019, 2022) to be capable of

accurately capturing important phenomena such as boundary layer and shear layer transition. Equations (1)–(3) are solved using the finite-volume framework, and the convective derivatives are discretised using a blended scheme (75% central differencing and 25% second-order upwind), which was revealed by Smith and Ventikos (2019) to be more stable than pure central differencing but without being overly dissipative. A three-point backward scheme is used for the temporal derivatives.

The acoustic source terms are interpolated from the fluid domain to the acoustic domain using radial basis function interpolation. This uses a scale-invariant multiquadric basis function that was proposed in Smith and Ventikos (2022) and shown to be a very accurate and stable interpolation method for this task, exhibiting excellent convergence characteristics.

The acoustic perturbation equations are given in Eqs. (4) and (5). These are a system of four linear hyperbolic equations for the acoustic pressure and velocity fluctuations, p_a and U_{a_i}. The approach assumes a constant mean density, ρ_0, and accounts for mean convection effects through the velocity term, $\overline{U_i}$. The source terms derived from the incompressible flow field are given on the right-hand-side of Eq. (4) as

$$\frac{\partial p_a}{\partial t} + \bar{U}_i \frac{\partial p_a}{\partial x_i} + \rho_0 c_0^2 \frac{\partial u_{a_i}}{\partial x_i} = -\frac{\partial \bar{p}}{\partial t} - \bar{U}_i \frac{\partial \bar{p}}{\partial x_i}, \tag{4}$$

$$\frac{\partial u_{a_i}}{\partial t} + \bar{U}_i \frac{\partial u_{a_i}}{\partial x_j} + \frac{1}{\rho_0}\frac{\partial p_a}{\partial x_j} = \mathbf{0}. \tag{5}$$

As with the fluid equations, the acoustic perturbation equations are solved using the finite volume framework. An exact Riemann solver is used with linear reconstruction for the face fluxes. The Riemann solver is used together with an explicit third-order strong stability preserving Runge-Kutta scheme for the temporal derivatives to solve the acoustic perturbation equations. To prevent unwanted wave reflections off of the far-field boundaries, a perfectly matched layer (PML) is used. First proposed by Berenger (1994) for
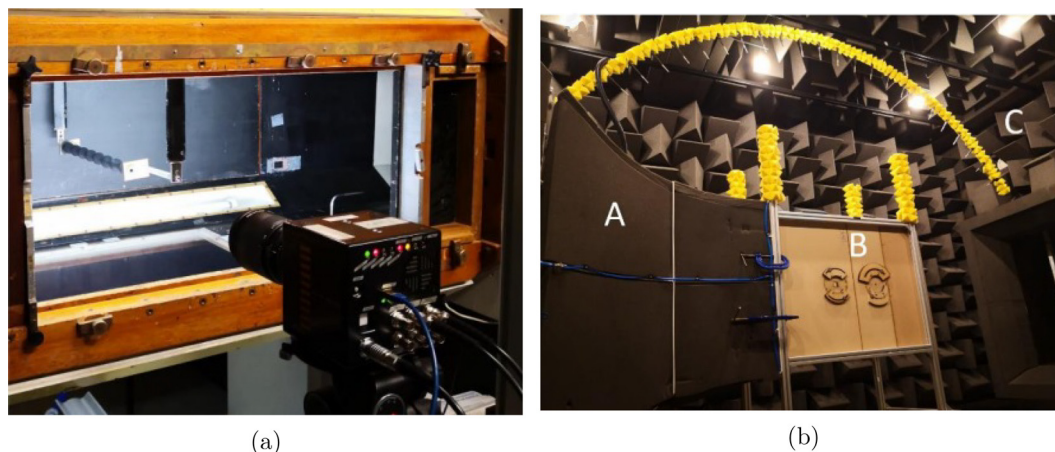
(a)

(b)

FIG. 2. (Color online) (a) Image of the closed-circuit wind tunnel with the PIV setup and (b) the anechoic wind tunnel showing (A) nozzle, (B) test section, and (C) far-field with microphone array.

J. Acoust. Soc. Am. **154** (3), September 2023

Smith *et al*.   1587

electromagnetic problems, this modifies the governing equations in a region close to the boundary to attenuate the incoming waves. This technique is highly effective and widely used in computational aeroacoustics (Hu, 1996, 2008), and a description of the implementation used in this work can be found in Smith and Ventikos (2022).

The fluid and acoustic domains (see Fig. 3) and meshes are quite different, reflecting the different physical phenomena that they need to capture. The fluid domain extends 20 cylinder diameters upstream of the geometry, 50 cylinder diameters downstream, and 40 cylinder diameters in the y-direction. The geometry has a span of ten cylinder diameters and is bounded at either end in the z-direction by symmetry planes. This is performed to represent the experimental configuration more closely, as opposed to using periodic boundaries that would mimic a geometry with an infinite span more closely. The inlet uses a fixed-velocity boundary condition, and a zero-gradient condition is imposed on the outlet. The acoustic domain extends 100 cylinder diameters in every direction from the geometry with the PML starting at a radius $r_0 = 1.8$ m from the centre of the domain. The two partially overlapping domains are displayed in Fig. 3, together with the start of the PML region, which then extends to the edges of the acoustic domain.

The fluid mesh is block structured and consists of 41.8×10^6 hexahedral cells. There are 480 cells around the geometry in the x–y plane and 300 cells along the span in the z-direction. The acoustic mesh is designed to ensure adequate resolution for the acoustic waves to propagate without numerical dissipation with additional refinement in the near-field to ensure accurate interpolation of the source terms from the fluid domain. Previous work (Smith and Ventikos, 2022) has shown that approximately 30 cells per acoustic wavelength are needed for this, and the grid resolution used here allows for the resolution of acoustic waves up to 680 Hz, which is equivalent to a Strouhal number of 0.6, without any numerical dissipation. Waves with frequencies much above this will attenuate more rapidly due to numerical dissipation. The resulting acoustic mesh has 7.2×10^6
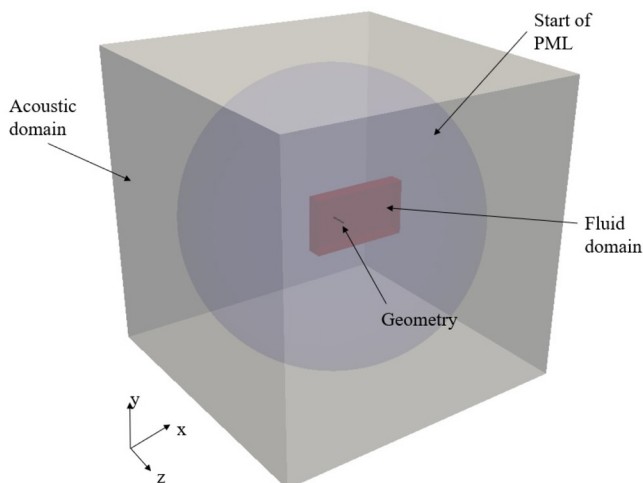

FIG. 3. (Color online) Illustration of the fluid and acoustic domains.

cells. Time steps for both parts of the simulation are chosen to ensure the Courant number is below one. The simulations are run for a duration equal to 100 cylinder shedding cycles, where data are sampled from 10 shedding cycles onward to ensure that the flow field has developed from the initial conditions. The data used in the subsequent analysis have been obtained at 50 kHz and a spatial resolution of 1 mm.

III. RESULTS

To begin with, an overview of the results is presented, including comparisons between experiments and the simulations for the mean flow field and far-field sound pressure level (SPL). It should be noted that unless otherwise stated, results presented are from the simulations. The lift and drag were not measured during the experiments and, therefore, the simulation data have been compared to data from the literature to provide additional confidence. Table II shows the Strouhal number, mean drag, and root-mean-square lift coefficient for the CC together with data from published sources. As can be observed, the values from the simulation are in good agreement with the experimental data. The mean drag coefficient for the vibrissa is significantly lower, with $\bar{C}_D = 0.44$, and the fluctuating lift is also much reduced when compared with the CC, with $C'_L = 0.02$. These values have been non-dimensionalised using the same parameters as used for the CC to facilitate a direct comparison between the two.

The mean streamwise velocities at midspan for the CC and at a nodal and saddle plane for the SVSC are shown in Fig. 4 for the experiments and simulations. In the experiments, velocity measurements were taken downstream of the geometry, but the flow around whole geometry is presented for the simulation. The agreement between the experimental data and simulation is generally very good. The velocity of the reversed flow in the wake of the cylinder is well predicted by the simulation, although the overall size of the recirculation region is smaller. For the SVSC, the experiment and simulation show a larger separated region at the saddle plane compared to the nodal plane. It can also be observed that magnitude of the reversed flow is much larger behind a saddle plane compared to that for a nodal plane because of the higher level of separation.

The acoustic spectra have been obtained from the experiments and simulations at 1.75 m above the mid-span of each geometry. For the experiments, background noise measurements have also been obtained. Due to the

TABLE II. Comparison of Strouhal number, mean drag, and fluctuating lift for the CC with published experimental data.

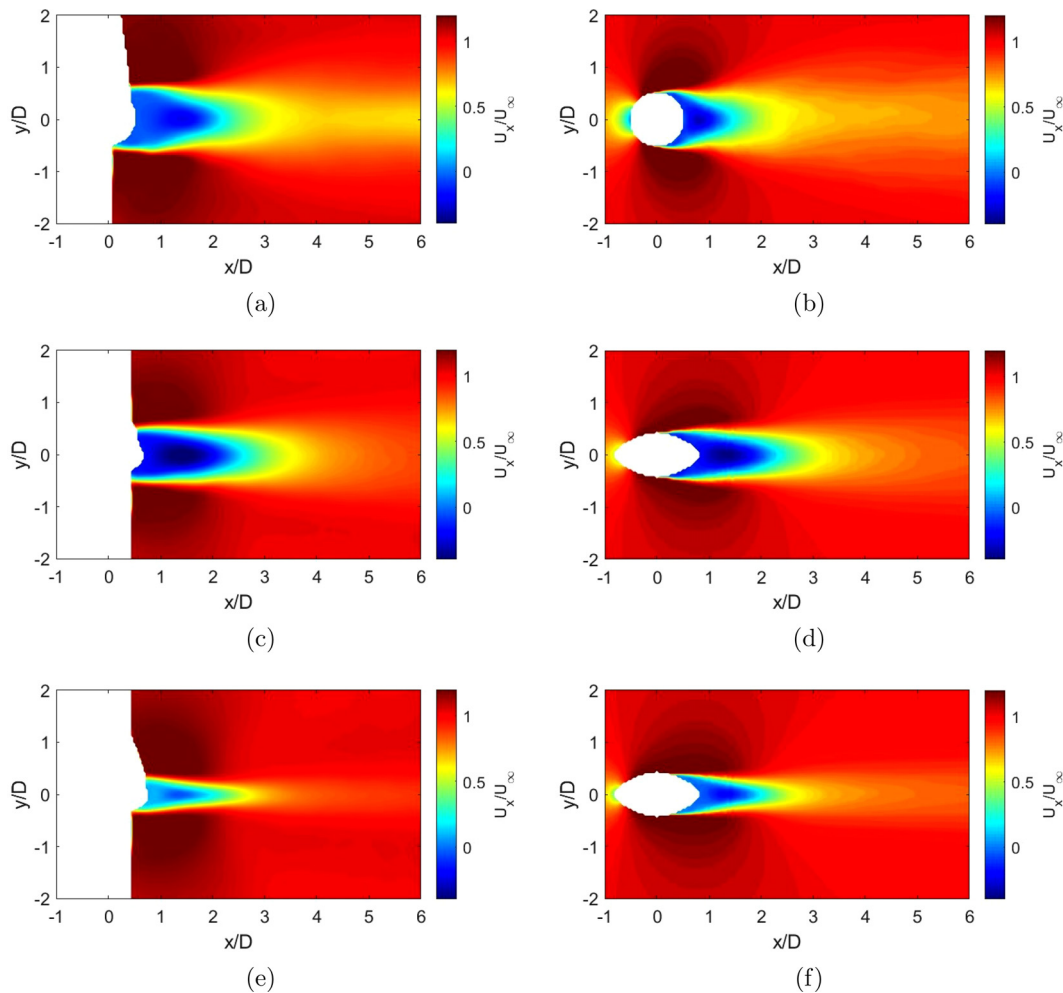| Source	Re	S_t	$\bar{C}_D$	C'_L
Simulation	3.7×10^4	0.19	1.28	0.40
Experiment	3.7×10^4	0.19	—	—
Szepessy and Bearman (1992)	4.3×10^4	0.19	1.0–1.3	0.4–0.7
Norberg (2003)	6.1×10^4	0.19	—	0.5
Cantwell and Coles (1983)	14×10^4	0.19	1.0–1.35	0.3–0.4

FIG. 4. (Color online) Mean streamwise flow for (a) CC experiment, (b) CC simulation, (c) SVSC saddle experiment, (d) SVSC saddle simulation, (e) SVSC nodal experiment, and (f) SVSC nodal simulation.

difference in the span used for the simulation, it is necessary to make a correction to the SPL to make a direct comparison with the experimental data. The span is greater than the correlation length and, hence, the correction method proposed by Kato *et al.* (1993) can be used:

$$\text{SPL}' = \text{SPL}_s + 10\,\log_{10}\left(\frac{L_e}{L_s}\right), \tag{6}$$

where L_e denotes the experimental span and L_s denotes the simulation span. This leads to a correction of $+3.0$ dB. The acoustic spectra for the two geometries are given in Fig. 5. For the CC, SPL is dominated by a narrowband component at the Strouhal shedding frequency, $S_t = 0.19$. Excellent agreement is noted between the experimental and computational results, with the peak shedding amplitude and frequency in good agreement. The SPL for the SVSC is markedly lower across all frequencies. Indeed, it is so low that it barely exceeds the background noise levels in the anechoic wind tunnel. Due to the closeness of the far-field acoustic results and background noise in the wind tunnel, the experimental data are not used for validation of the simulation for the SVSC. The experimental results exceed the

background noise more notably in the range $0.2 \leq S_t \leq 0.5$, and a broadband hump is observed centred around $S_t = 0.28$, which agrees with the peak of the broadband hump shown in the simulation results. There is no pronounced peak in the spectra for this geometry indicating a significant change in the noise generating mechanism for the SVSC when compared to the CC. As well as a lack of a distinct narrowband component, the simulation also shows a reduction in high frequency noise for the SVSC compared to that with the CC, particularly for $S_t > 1.0$. The reduction in the noise at higher frequencies is attributed to lower fluctuation intensities on the surface and in the wake of the SVSC, as will be shown in subsequent analysis. This leads to a reduction in turbulent kinetic energy with the smaller scales associated with the higher frequencies being much less energetic.

The extent of the differences in the overall SPL can clearly be seen in the directivity plot given in Fig. 6. The overall SPL is obtained by integrating from $S_t = 0.1$ to $S_t = 2.0$. Here, $\theta = 0°$ denotes downstream and $180°$ is upstream of the geometry. Whilst both geometries exhibit a dipolar acoustic field with higher sound levels directly above and below, the overall level for the SVSC is
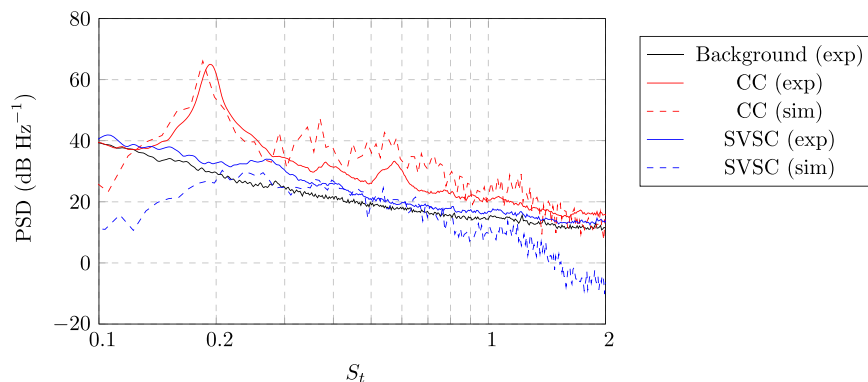
J. Acoust. Soc. Am. **154** (3), September 2023

Smith *et al.*   1589

FIG. 5. (Color online) Power spectral density (PSD) of the SPL for the CC and SVSC.

significantly lower at all angles. At 90°, which is directly above the geometries, the overall SPL for the SVSC is 24.3 dB lower than that for the CC. The dipolar pattern indicates that the noise generation mechanism is still linked to fluctuations in the lift force on the SVSC, but the reduction in the overall level and lack of a clear tonal peak indicate substantial differences in the underlying flow and, hence, noise generating mechanisms for the two geometries. Experimental data for the CC are also depicted here, again indicating good agreement with the simulation at all measured angles. Note that the experimental data for the SVSC has not been included because the overall SPL was too close to the background noise levels and, therefore, a comparison between this and the simulation is not valid here.

Important insights into these differences can be gained by considering how the instantaneous velocity field changes and how this relates to the time-varying lift coefficient. The noise from the flow over a bluff body at low Mach number is related to the time-varying lift force (Gerrard, 1955; Phillips, 1956) and, so, understanding how this changes is crucial to understanding the differences between the CC and SVSC. In Figs. 7 and 8, the lift coefficient over ten shedding cycles (of the CC) is shown for both geometries together with the instantaneous streamwise velocity at two selected

time instances. For the CC, we see the typical behaviour of a periodic lift coefficient associated with alternating vortex shedding. The vortex shedding leads to high and low pressure alternately on the upper and lower surfaces, thus, creating an oscillatory lift force. These alternately high and low pressures are also what create the dipole-type sound. Locations (a) and (b) in Fig. 7 denote minima and maxima for the lift, and the flow field at these locations shows vortices shedding from each side of the cylinder at these two instanced. This process can clearly be seen in the animation in Mm. 1.

Mm. 1. Lift coefficient over ten shedding cycles for the CC together with the instantaneous streamwise velocity and pressure fields at mid-span.

Figure 8 shows a very different behaviour for the SVSC. First, the lift fluctuations are an order of magnitude smaller than they are for the CC, and the oscillations are far less regular. What is also apparent from Fig. 8 is that the alternating vortex shedding observed for the CC is absent from the SVSC flow. The fluctuations of the lift coefficient are significantly smaller for the SVSC and far less periodic. Instead of the usual alternating vortices, there are smaller less coherent structures being shed from a more stable wake region. As with the CC, the dynamics are most clearly observed in the animation of Mm. 2. As was shown in Fig. 4, the wake at the nodal plane is clearly narrower than that at the saddle plane. The reduction in the fluctuation intensity translates into a reduction in the levels of turbulent kinetic energy in the wake, which also helps to explain why the higher frequency noise is also significantly lower for the SVSC as compared to that for the CC. It is interesting to compare these results to the experimental data of Chen et al. (2022b), who considered the CC and SVSC alongside an EC. This study showed that the EC has a slightly lower overall SPL, but the fundamental noise generating mechanism remains the same as that for the CC. The slenderer EC does exhibit weaker vortex shedding than the CC, which manifests as a lower peak in SPL at the Strouhal shedding frequency, but the acoustic field is still dominated by the alternating vortex shedding that we see for the CC.
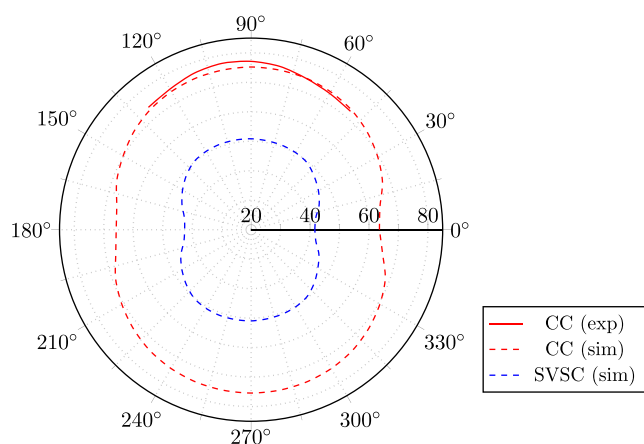

FIG. 6. (Color online) Directivity pattern for overall SPL (dB) obtained from the simulations for the CC and vibrissa shaped cylinder.
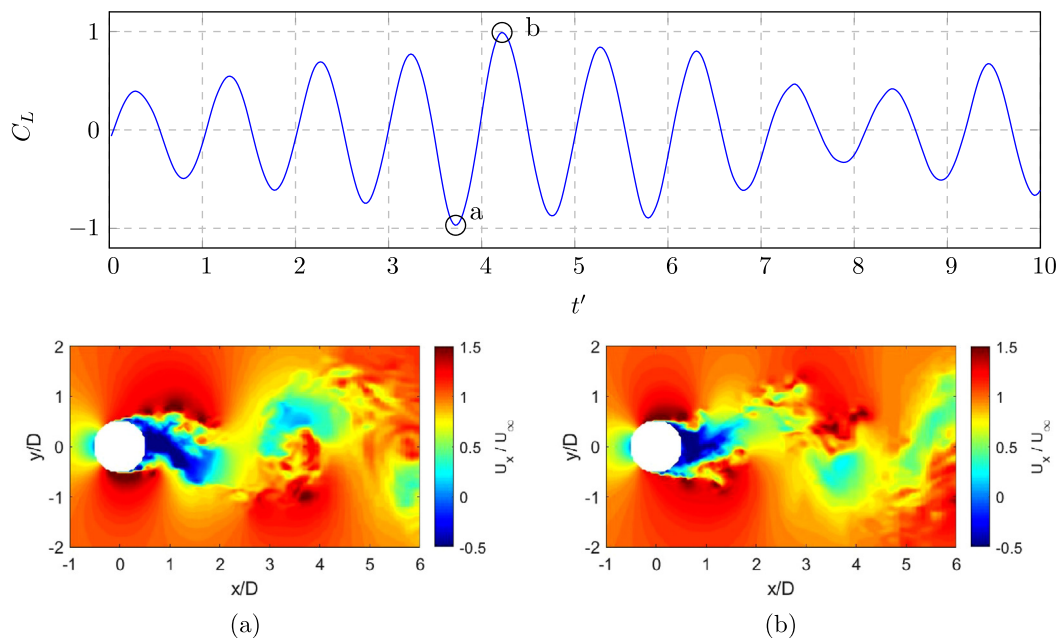
Smith *et al.*

FIG. 7. (Color online) Lift coefficient for the CC over ten shedding cycles together with the instantaneous streamwise velocity field at mid-span for points (a) and (b).
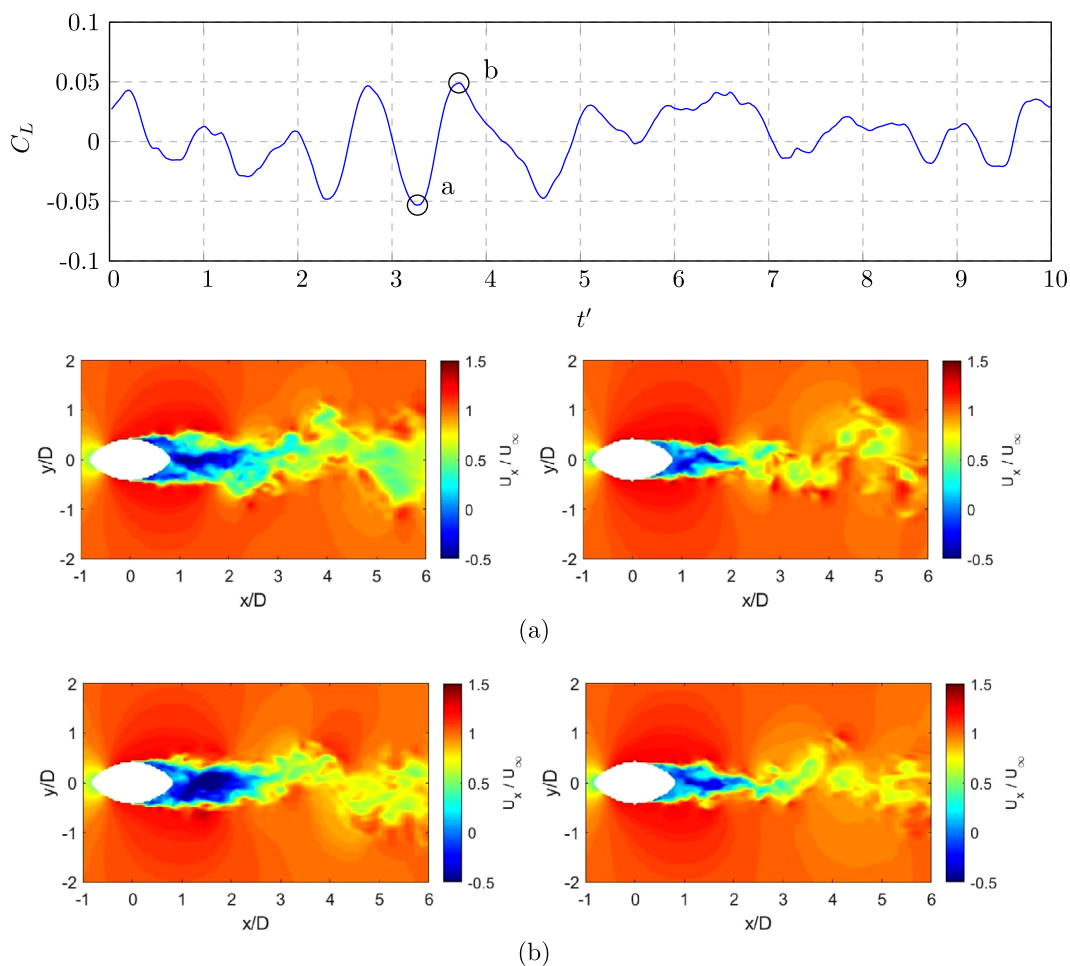

FIG. 8. (Color online) Lift coefficient for the SVSC over ten shedding cycles together with instantaneous streamwise velocity contour plots for points (a) and (b). The left plots are at a saddle plane and the right plots are for a nodal plane.

Therefore, the significant change in SPL for the SVSC is not due to weaker shedding as a result of the SVSC being more slender than the CC, but a fundamental change in the vortex shedding dynamics.

Mm. 2. Lift coefficient over ten shedding cycles for the SVSC together with the instantaneous streamwise velocity and pressure fields at a nodal plane and a saddle plane.

The change in the vortex shedding pattern for the SVSC is confirmed by considering the fluctuations in the surface pressure coefficient on the upper and lower sides of the geometry. In Fig. 9, these are shown at $\theta = 60°$ and $\theta = 300°$, again, over ten CC shedding cycles (note that $\theta = 0°$ denotes the downstream-most point). For the CC, the pressure fluctuations are strongly out-of-phase with a correlation coefficient of –0.90 for the pressure fluctuations at these two points. This contrasts sharply with that of the SVSC, which shows almost no correlation between the fluctuations on the two sides of the geometry. At the saddle plane, the correlation coefficient is 0.03 and at the nodal plane, the correlation coefficient is 0.12. We may, therefore, deduce that the flow on the two sides of the geometry is uncorrelated, which helps to explain the lack of a dominant narrowband component in the acoustic spectrum.
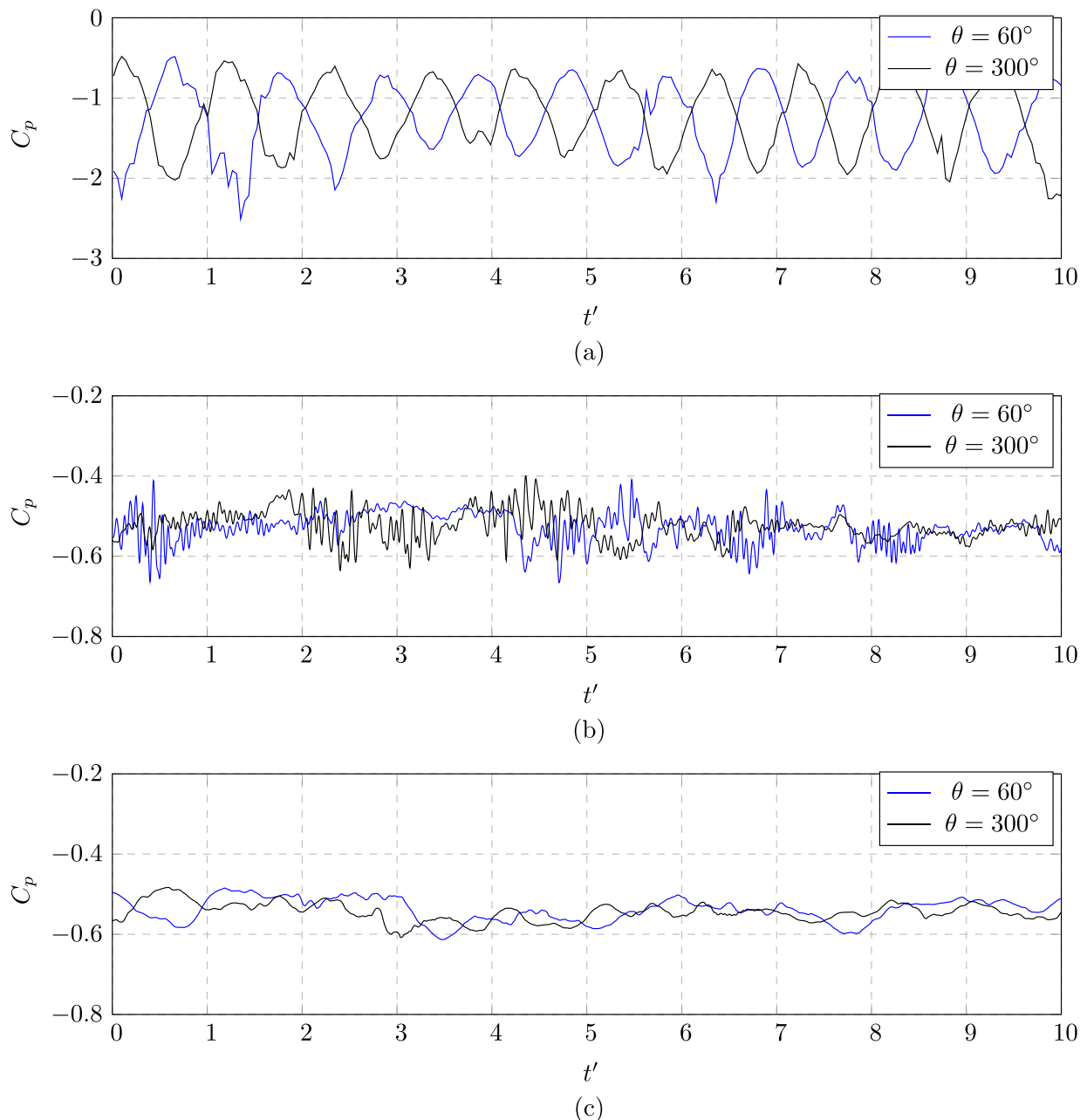

FIG. 9. (Color online) Pressure coefficient over ten shedding cycles at $\theta = 60°$ and $\theta = 300°$ for (a) CC at mid-span, (b) SVSC at a saddle plane, and (c) SVSC at a nodal plane.
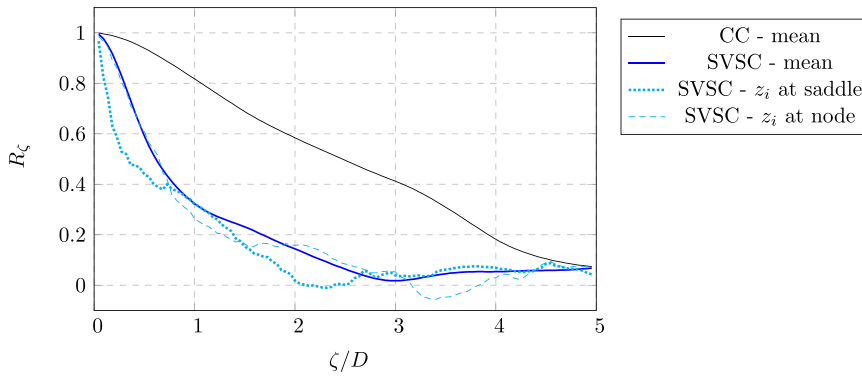
FIG. 10. (Color online) Spanwise correlation coefficient for both geometries for a separation distance ζ/D. The mean curves have been computed as per Eq. (7), whereas the other curves use a single starting point, z_i, as defined in the legend.

As well as the lack of correlation between the two sides, the spanwise correlation is also significantly lower for the SVSC. Figure 10 shows this for both geometries for various separations, $\zeta = |z_j - z_i|$. Due to the geometric variation along the span for the SVSC, this has been computed using an average. For each separation distance, ζ, the correlation coefficient has been computed using $N = 50$ different starting locations, z_i, along the span, resulting in 50 different correlation curves. These are then averaged, ensuring that the correlation coefficient reflects the mean behaviour across the span and removes any bias from starting in a particular location (e.g., at a nodal plane as opposed to a saddle plane). This leads to the following equation for R_ζ:

$$R_\zeta = \frac{1}{N} \sum_{i=1}^{N} \frac{\overline{p(z_i)p(z_i + \zeta)}}{\sqrt{\overline{p^2(z_i)} \, \overline{p^2(z_i + \zeta)}}}, \qquad (7)$$

where $\overline{p^2}$ denotes the mean-square pressure. The correlation coefficient is also shown for z_i at a nodal plane and z_i at a saddle plane for comparison. Thus, these are not mean values but illustrate the change in the correlation coefficient depending on the starting location. Once again, the correlation of the SVSC is much lower than that of the CC, reducing by half in little over $0.5D$, compared to the CC, which reduces by half after $2.5D$. This further explains why the acoustic intensity is so much lower for the SVSC. In addition to the lack of large coherent shedding in the x-y plane, there is little correlation in the spanwise direction, resulting in the geometry behaving as a very weak acoustic source.

To confirm the relationship between the pressure fluctuations on the surface and far-field noise, frequency and coherence analysis has been conducted using the surface pressure fluctuations at $\theta = 60°$. Figure 11 shows the power spectral density of the surface pressure fluctuations for both geometries at a series of points along the span. For the CC, a clear narrowband component is visible at the $S_t = 0.19$, and spectra are reasonably constant along the span. This is consistent with the acoustic results in Fig. 5 and our understanding of flow-induced noise for cylinders. For the SVSC, the power spectral density (PSD) shows much lower amplitudes across the entire frequency range, again, mirroring the acoustic spectra in Fig. 5. This also shows a clear spanwise variation coinciding with the variation in the geometry. There are four distinct areas where the amplitude remains higher across a broad frequency range. The midpoint of each of these corresponds to a saddle plane, and it is clear that the intensity of the fluctuations is much higher than at the nodal planes, which are located where the fluctuations are lowest. This result echoes that shown in Fig. 9, which too showed fluctuations with a higher amplitude and higher frequency at a saddle plane compared to a nodal plane. Additionally, this shows that the reduction in higher
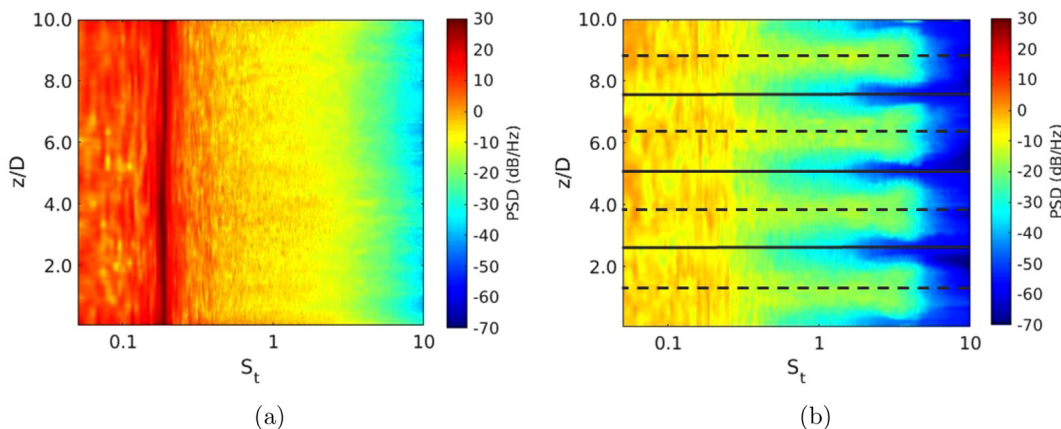

FIG. 11. (Color online) Power spectral densities of the surface pressure fluctuations at $\theta = 60°$ along the span of (a) CC and (b) SVSC. The dotted lines denote saddle planes, and the solid lines denote nodal planes for the SVSC.

frequency noise observed in Fig. 5 is more the result of changes in the flow at the nodal planes than those at the saddle planes.

Finally, the coherence of the surface pressure fluctuations with the far-field acoustic pressure is presented in Fig. 12. This shows the magnitude-squared coherence, γ^2, between the surface pressure fluctuations at $\theta = 60°$ and far-field pressure 1.75 m above each geometry. The surface pressure points are the same used for the frequency analysis in Fig. 11. The magnitude-squared coherence has been computed for each pair using the Welch method with a Hamming window and a 50% overlap for each window. For the CC, a strong coherence is seen at the Strouhal frequency, again, confirming the link between this process and the far field noise. It is noted that the coherence reduces for points closer to the top and bottom of the cylinder and most likely due to the boundary conditions imposed in the simulation. Figure 11 shows that the same shedding pattern still occurs at the ends, but the lack of coherence with the far-field noise suggests that the boundaries do affect the scattering of the pressure fluctuations as acoustic waves. What this means in practice is that the vortex shedding close to the ends contributes less to the far-field noise at the Strouhal shedding frequency than the vortex shedding closer to mid-span. However, the boundary conditions were chosen to more closely reflect the experimental setup, where the cylinder was pinned at either end by plates. Given the closeness of the far-field sound levels for the experiment and simulation, it is reasonable to conclude that such effects were also present in the experiment.

For the SVSC, we see a much lower coherence. However, the highest coherence values do occur at the frequency range where far-field SPL is elevated, as depicted in Fig. 5. Unlike the surface pressure fluctuations in Fig. 11, there is very little relationship between the coherence and geometry variation along the span for the SVSC. This reduced coherence and lack of relationship with the geometry shows that only a weak relationship exists between the strength of the pressure fluctuations at the surface and that of the far-field noise. This is due to the three-dimensional nature of the flow as compared to the CC. Previous analysis in this paper has illustrated that the spanwise correlation is much reduced for the SVSC, and there is little correlation between the pressure fluctuations on the two sides. This leads to much higher levels of interference between the fluctuations which make up the acoustic source terms, reducing the coherence between what happens close to the surface and the far-field noise. These effects all combine to make the SVSC a far less efficient acoustic source than a CC across the entire frequency range.

IV. CONCLUSIONS

In this work, the aeroacoustic performance of a SVSC has been compared to a CC at a $Re = 3.7 \times 10^4$ using experimental and computational methods. Data obtained from wind tunnel testing have been used to validate simulations performed using a hybrid aeroacoustic model, providing confidence in the methodology, as well as detailed insights into the flow physics and resulting noise.

The results show that the noise produced by the flow over the SVSC is significantly lower than that for the CC. At a distance of 1.75 m from the geometry, the overall SPL is 24.3 dB lower for the SVSC, and no narrowband peak is observed. Several fundamental changes in the fluid dynamics have been identified that explain the behaviour. First, the large anti-phase vortex shedding typically associated with bluff body flows is absent in the case of the SVSC. Instead, there is a more stable wake region with smaller uncorrelated vortices shedding from either side of the geometry. The lack of correlation between the top and bottom is combined with a very low spanwise correlation, leading to a significantly weaker acoustic intensity with no dominant tonal or narrowband component.

These results show that a geometry incorporating the features of the harbour seal vibrissa could be highly effective at reducing flow-induced noise. Tonal noise can be completely eliminated, leading to a broadband sound field with a lower intensity across all frequencies and all directions. Potential applications for such a design include aircraft landing gear, train pantographs, and other bluff bodies
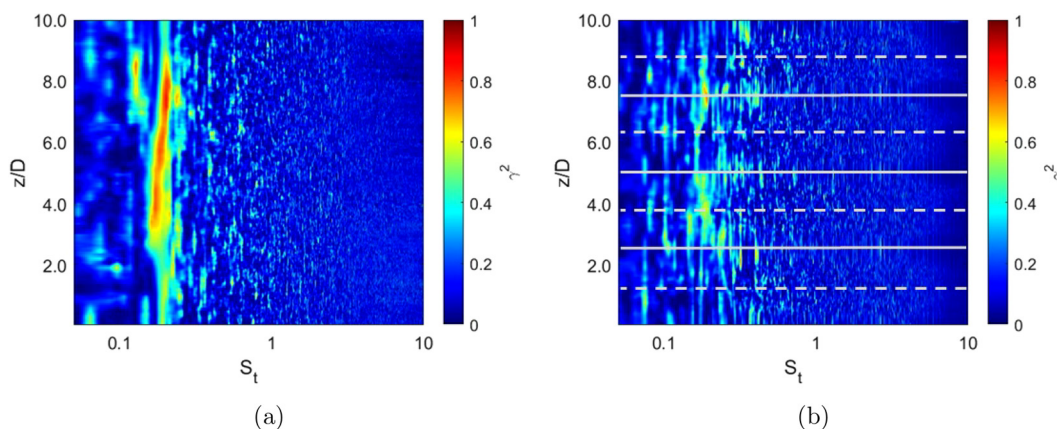

FIG. 12. (Color online) Magnitude-squared-coherence between the surface pressure fluctuations at $\theta = 60°$ and the far-field acoustic pressure for (a) CC and (b) SVSC. The dotted lines denote saddle planes, and the solid lines denote nodal planes for the SVSC.

1594   J. Acoust. Soc. Am. **154** (3), September 2023

Smith *et al.*

that produce undesirable noise, such as struts used on some aircraft and marine vessels. Future research should consider the performance of the SVSC in different conditions, particularly in the critical and trans-critical regimes (Re $> 1.5 \times 10^5$) to demonstrate the suitability of this geometry to a wider range of applications. Research could also consider whether such a modification could be applied to elliptical airfoil geometries. Given that vibrissa shaped cylinders are quieter than ECs, it would be of interest to see the effect of a vibrissa shaped elliptical lifting surface on separation and trailing edge noise.

ACKNOWLEDGMENTS

Agrawal, B. R., and Sharma, A. (**2016**). "Numerical analysis of aerodynamic noise mitigation via leading edge serrations for a rod–airfoil configuration," Int. J. Aeroacoust. **15**(8), 734–756.

Berenger, J.-P. (**1994**). "A perfectly matched layer for the absorption of electromagnetic waves," J. Comput. Phys. **114**(2), 185–200.

Cantwell, B., and Coles, D. (**1983**). "An experimental study of entrainment and transport in the turbulent near wake of a circular cylinder," J. Fluid Mech. **136**, 321–374.

Chaitanya, P., Joseph, P., Narayanan, S., and Kim, J. (**2018**). "Aerofoil broadband noise reductions through double-wavelength leading-edge serrations: A new control concept," J. Fluid Mech. **855**, 131–151.

Chen, G., Liu, X., Zang, B., and Azarpeyvand, M. (**2022a**). "The effect of the splitter plate on the aeolian tone mitigation," in *28th AIAA/CEAS Aeroacoustics 2022 Conference*, Southampton, UK (AIAA, Reston, VA), p. 3094.

Chen, G., Liu, X., Zang, B., and Azarpeyvand, M. (**2022b**). "The effect of the vibrissa shaped cylinder on the aeolian tone mitigation," in *51st International Congress and Exposition on Noise Control Engineering*, Glasgow, UK (Institute of Noise Control Engineering, Reston, VA), pp. 1–8.

Chen, W., Qiao, W., Tong, F., Wang, L., and Wang, X. (**2018**). "Numerical investigation of wavy leading edges on rod–airfoil interaction noise," AIAA J. **56**(7), 2553–2567.

Chu, S., Xia, C., Wang, H., Fan, Y., and Yang, Z. (**2021**). "Three-dimensional spectral proper orthogonal decomposition analyses of the turbulent flow around a seal-vibrissa-shaped cylinder," Phys. Fluids **33**(2), 025106.

Clark, I. A., Daly, C. A., Devenport, W., Alexander, W. N., Peake, N., Jaworski, J. W., and Glegg, S. (**2016**). "Bio-inspired canopies for the reduction of roughness noise," J. Sound Vib. **385**, 33–54.

Fujita, H. (**2010**). "The characteristics of the aeolian tone radiated from two-dimensional cylinders," Fluid Dyn. Res. **42**(1), 015002.

Gerrard, J. H. (**1955**). "Measurements of the sound from circular cylinders in an air stream," Proc. Phys. Soc. B **68**(7), 453–461.

Graham, R. R. (**1934**). "The silent flight of owls," Aeronaut. J. **38**(286), 837–843.

Hanke, W., Witte, M., Miersch, L., Brede, M., Oeffner, J., Michael, M., Hanke, F., Leder, A., and Dehnhardt, G. (**2010**). "Harbor seal vibrissa morphology suppresses vortex-induced vibrations," J. Exp. Biol. **213**(15), 2665–2672.

Hu, F. Q. (**1996**). "On absorbing boundary conditions for linearized Euler equations by a perfectly matched layer," J. Comput. Phys. **129**(1), 201–219.

Hu, F. Q. (**2008**). "Development of PML absorbing boundary conditions for computational aeroacoustics: A progress review," Comput. Fluids **37**(4), 336–348.

Inoue, O., and Hatakeyama, N. (**2002**). "Sound generation by a two-dimensional circular cylinder in a uniform flow," J. Fluid Mech. **471**, 285–314.

Jacob, M. C., Boudet, J., Casalino, D., and Michard, M. (**2005**). "A rod-airfoil experiment as a benchmark for broadband noise modeling," Theor. Comput. Fluid Dyn. **19**(3), 171–196.

Jie, H., and Liu, Y. Z. (**2017**). "Large eddy simulation and proper orthogonality decomposition of turbulent flow around a vibrissa-shaped cylinder," Int. J. Heat Fluid Flow **67**, 261–277.

Kato, C., Iida, A., Takano, Y., Fujita, H., and Ikegawa, M. (**1993**). "Numerical prediction of aerodynamic noise radiated from low Mach number turbulent wake," in *31st Aerospace Sciences Meeting*, Reno, NV (AIAA, Reston, VA), p. 145.

Kim, W.-W., and Menon, S. (**1995**). "A new dynamic one-equation sub-grid-scale model for large eddy simulations," in *33rd Aerospace Sciences Meeting and Exhibit*, Reno, NV (AIAA, Reston, VA), p. 356.

Liu, X., Chen, G., Zang, B., and Azarpeyvand, M. (**2022**). "An experimental study of aerodynamic noise of the wavy and vibrissa shaped cylinders," in *28th AIAA/CEAS Aeroacoustics 2022 Conference*, Southampton, UK (AIAA, Reston, VA), p. 2982.

Mayer, Y. D., Jawahar, H. K., Szőke, M., Ali, S. A. S., and Azarpeyvand, M. (**2019**). "Design and performance of an aeroacoustic wind tunnel facility at the university of Bristol," Appl. Acoust. **155**, 358–370.

Norberg, C. (**2003**). "Fluctuating lift on a circular cylinder: Review and new measurements," J. Fluids Struct. **17**(1), 57–96.

Phillips, O. (**1956**). "The intensity of aeolian tones," J. Fluid Mech. **1**(6), 607–624.

Rayleigh, J. W. S. B. (**1896**). *The Theory of Sound* (MacMillan, London), Vol. 2.

Revell, J. D., Prydz, R. A., and Hays, A. P. (**1978**). "Experimental study of aerodynamic noise vs drag relationships for circular cylinders," AIAA J. **16**(9), 889–897.

Smith, T. A., and Klettner, C. A. (**2022**). "Airfoil trailing-edge noise and drag reduction at a moderate Reynolds number using wavy geometries," Phys. Fluids **34**(11), 117107.

Smith, T. A., and Ventikos, Y. (**2019**). "Boundary layer transition over a foil using direct numerical simulation and large eddy simulation," Phys. Fluids **31**(12), 124102.

Smith, T. A., and Ventikos, Y. (**2022**). "A hybrid computational aeroacoustic model with application to turbulent flows over foil and bluff bodies," J. Sound Vib. **526**, 116773.

Szepessy, S., and Bearman, P. W. (**1992**). "Aspect ratio and end plate effects on vortex shedding from a circular cylinder," J. Fluid Mech. **234**, 191–217.

Wagner, H., Weger, M., Klaas, M., and Schröder, W. (**2017**). "Features of owl wings that promote silent flight," Interface Focus **7**(1), 20160078.

Wang, J., Zhang, C., Wu, Z., Wharton, J., and Ren, L. (**2017**). "Numerical study on reduction of aerodynamic noise around an airfoil with biomimetic structures," J. Sound Vib. **394**, 46–58.

Wang, L., Liu, X., and Li, D. (**2021**). "Noise reduction mechanism of airfoils with leading-edge serrations and surface ridges inspired by owl wings," Phys. Fluids **33**(1), 015123.

Wang, S., and Liu, Y. (**2016**). "Wake dynamics behind a seal-vibrissa-shaped cylinder: A comparative study by time-resolved particle velocimetry measurements," Exp. Fluids **57**, 1–20.

Yoon, H. S., Nam, S. H., and Kim, M. I. (**2020**). "Effect of the geometric features of the harbor seal vibrissa based biomimetic cylinder on the flow over a cylinder," Ocean Eng. **218**, 108150.

21 September 2023 11:43:44

J. Acoust. Soc. Am. **154** (3), September 2023

Smith *et al.*   1595